

# The Circumstellar Disk of the Be Star *o* Aquarii

T. A. A. Sigut,<sup>1,2</sup> C. Tycner,<sup>3</sup> B. Jansen,<sup>3</sup> R. T. Zavala<sup>4</sup>

Accepted for publication in the Astrophysical Journal

## ABSTRACT

Omicron Aquarii is late-type, Be shell star with a stable and nearly symmetric H $\alpha$  emission line. We combine H $\alpha$  interferometric observations obtained with the Navy Precision Optical Interferometer (NPOI) covering 2007 through 2014 with H $\alpha$  spectroscopic observations over the same period and a 2008 observation of the system's near-infrared spectral energy distribution to constrain the properties of *o* Aqr's circumstellar disk. All observations are consistent with a circumstellar disk seen at an inclination of  $75 \pm 3^\circ$  with a position angle on the sky of  $110 \pm 8^\circ$  measured E from N. From the best-fit disk density model, we find that 90% of the H $\alpha$  emission arises from within 9.5 stellar radii, and the mass associated with this H $\alpha$  disk is  $\sim 1.8 \times 10^{-10}$  of the stellar mass and the associated angular momentum, assuming Keplerian rotation for the disk, is  $\sim 1.6 \times 10^{-8}$  of the total stellar angular momentum. The occurrence of a central quasi-emission (CQE) feature in Mg II  $\lambda 4481$  is also predicted by this best-fit disk model and the computed profile compares successfully with observations from 1999. To obtain consistency between the H $\alpha$  line profile modelling and the other constraints, it was necessary in the profile fitting to weight the line core (emission peaks and central depression) more heavily than the line wings, which were not well reproduced by our models. This may reflect the limitation of assuming a single power-law for the disk's equatorial density variation. The best-fit disk density model for *o* Aqr predicts that H $\alpha$  is near its maximum strength as a function of disk density, and hence the H $\alpha$  equivalent width and line profile change only weakly in response to large (factor of  $\sim 5$ ) changes in the disk density. This may in part explain the remarkable observed stability of *o* Aqr's H $\alpha$  emission line profile.

*Subject headings:* techniques: interferometric – stars: circumstellar matter – stars: emission line, Be – stars: individual (*o* Aqr)

## 1. Introduction

*o* Aqr (HR 8402, HD 209409) is a bright, Be shell star of spectral type B7IVe. Rivinius et al. (2006) note that *o* Aqr has had stable H $\alpha$  emission and does not exhibit  $V/R$  variations, thus excluding a prominent one-armed spiral density wave in the disk (Okazaki 1991; Hanuschik et al. 1995). However, *o* Aqr does possess a central quasi-emission feature (CQE) in Mg II  $\lambda 4481$  Rivinius et al. (2006), consistent with a high viewing angle for the disk (Hanuschik 1996). Stoeckley & Nuscombe (1987) used the shape and widths of He I  $\lambda 4471$  and Mg II  $\lambda 4481$  and a gravi-

tational darkening model for the central star to estimate the inclination angle for *o* Aqr, finding  $i > 82^\circ$ , consistent with its shell designation. Hubrig et al. (2009) claimed detection of a weak magnetic field in *o* Aqr of about 100 G at  $3\sigma$ ; however, Bagnulo et al. (2012) conclude that the polarization detected with the FORS1 VLT instrument was instrumental in nature. *o* Aqr is not known to have a binary companion, a result strengthened by direct AO imaging observations in the K-band with VLT (Oudmaijer & Parr 2010). The  $v \sin i$  of *o* Aqr is  $282 \text{ km s}^{-1}$ , giving a  $V/V_{\text{crit}}$  ratio of 0.74 (Touhami et al. 2013). This is consistent with the consensus that rapid rotation is a key driver behind the Be phenomena (Howarth 2007; Rivinius 2013; Rivinius et al. 2013).

As both bright ( $m_V = 4.69$ ) and close ( $d = 134 \text{ pc}$ ; based on *Hipparcos* parallax), *o* Aqr has been a target of recent interferometric studies. Meilland et al. (2012) included it in their survey of Be stars and Touhami et al. (2013) resolved it in the K-band, finding a major axis of  $1.525 \pm 0.642 \text{ mas}$  as measured by

<sup>1</sup>Department of Physics and Astronomy, The University of Western Ontario, London, Ontario, Canada N6A 3K7

<sup>2</sup>Centre for Planetary Science and Exploration, The University of Western Ontario, London, Ontario, Canada N6A 3K7

<sup>3</sup>Department of Physics, Central Michigan University, Mount Pleasant, MI 48859, USA

<sup>4</sup>US Naval Observatory, Flagstaff Station, 10391 W. Naval Observatory Rd., Flagstaff, AZ 86001

fitting a geometric star-plus-Gaussian disk to the observed visibilities.

Optical interferometry using  $H\alpha$  emission has proven to be very effective in resolving the circumstellar emission of Be stars. The strength of  $H\alpha$  can result in detectable emission extending to many stellar radii (Tycner et al. 2005; Grundstrom & Gies 2006). The combination of  $H\alpha$  interferometry and contemporaneous  $H\alpha$  spectroscopy has been shown to be a powerful tool to constrain the physical properties of Be star circumstellar disks (Tycner et al. 2008; Jones et al. 2008). In this current work, we attempt to constrain the physical parameters of the  $H\alpha$  emitting circumstellar disk surrounding *o* Aqr using this approach. We attempt to find a unified disk density model that reproduces the observed  $H\alpha$  emission profile,  $H\alpha$  interferometric visibilities, the near-IR spectral energy distribution, and the existence of a CQE in  $MgII \lambda 4481$ , all using the BEDISK (Sigut & Jones 2007) and BERAY (Sigut 2011) numerical codes.

## 2. Observations

### 2.1. Spectroscopy

Spectroscopic observations in the  $H\alpha$  region have been obtained using the Solar Stellar Spectrograph on the John S. Hall telescope at Lowell Observatory. Thirty individual spectra are available for observing seasons from 2005 through 2014. The raw echelle spectral frames have been processed using the standard reduction routines developed by Hall et al. (1994) for the instrument. The  $H\alpha$  profile of *o* Aqr is doubly-peaked, symmetric, and very stable over the time period considered. The stability of the  $H\alpha$  emission is important as our interferometric observations cover very similar time period (2007 through 2014), and we combine all available visibilities into a single analysis.

Figure 1 shows the mean profile with the  $1\sigma$  variation shown as the error bars. The lower panel of this figure also shows the  $H\alpha$  equivalent width (EW) as a function of Julian date over the nine year period covered by the observations. The mean EW is  $19.9 \text{ \AA}$ , with a  $1\sigma$  variation of only  $0.9 \text{ \AA}$  or  $4.5\%$ .<sup>1</sup> The profile has a peak-to-continuum contrast of 3.75, and the  $H\alpha$  shell parameter, defined as the ratio of the average flux in the emission peaks divided by the flux at line centre, is 2.2. This identifies *o* Aqr as a shell star following Hanuschik (1996): shell stars have ratios in excess of 1.5 based on the correlation of the  $H\alpha$  shell parameter with net, line-centre absorption in weak, optically thin

<sup>1</sup> We have additional  $H\alpha$  spectra from June 24, 2015 (JD=2457198) which is consistent with the profile and equivalent widths of Figure 1.

Table 1: Adopted stellar parameters for *o* Aqr

Parameter	Value
Mass <sup>a</sup> ( $M_{\odot}$ )	4.2
Radius <sup>a</sup> ( $R_{\odot}$ )	3.2
Luminosity ( $L_{\odot}$ )	$3.6 \times 10^2$
$T_{\text{eff}}$ (K)	14,000
$\log(g)$	4.0
Distance <sup>b</sup> (pc)	134
Angular Diameter (mas)	0.222

#### Notes.

<sup>a</sup> Adopted from Townsend et al. (2004).

<sup>b</sup> Based on *Hipparcos* parallax (Perryman et al. 1997).

Fe II lines (Hanuschik 1996). Typically for shell stars, the viewing inclination of the system is in excess of  $70^\circ$ .

Finally, Figure 1 shows that the emission in  $H\alpha$  extends to  $\approx \pm 400 \text{ km s}^{-1}$ . Using the adopted mass and radius for *o* Aqr from Table 1, the velocity at the inner edge of a Keplerian disk is  $\approx 500 \text{ km s}^{-1}$ . As the inclination of the system must be large and  $\sin i \approx 1$ , there is no evidence of disk emission beyond the velocities available in the disk. Note that this remains the case even if *o* Aqr were critically rotating (see discussion below); the disk would then start at  $1.5 R_*$  due to the geometric distortion caused by rapid rotation, and the velocity of the inner edge of the disk would drop to  $\approx 400 \text{ km s}^{-1}$ .

### 2.2. Interferometry

We have acquired interferometric observations of *o* Aqr using the Navy Precision Optical Interferometer (NPOI) on a total of 58 nights covering five observing seasons: 2007 Jun, 2011 Oct, 2012 Oct through Nov, 2013 Oct through Dec, and 2014 Jul. The NPOI is a long-baseline interferometer that can measure the fringe contrast between various telescope pairs (i.e., baselines) for up to 6 telescopes simultaneously (Armstrong et al. 1998). The fringe contrast represents the measure of the degree of coherence between the light beams from separate telescopes and when expressed as a squared visibility ( $V^2$ ) represents the normalized Fourier power of the brightness distribution of the source on the sky (Hummel 2008). Therefore, assuming the source is spatially resolved, it allows the angular extent of the source to be constrained.

The processing of NPOI data has been conducted using the OYSTER (Optical Interferometer Script Data Reduction) package developed by Christian Hummel, which follows the procedures outlined in Hummel et al. (1998) with additional bias corrections using off-fringe measurements (Hummel et al. 2003). Typically, for an unresolved point source on the sky, no

loss of fringe contrast would be expected; however, atmospheric and instrumental effects will contribute towards loss of coherence between light beams from separate telescopes. These effects are typically removed from the data by interleaving the observations of the target star with observations of a source of a known angular diameter (i.e., a calibrator star) that allows the determination of instrumental and atmospheric response functions, which in turn can be divided out of the data of the target star. However, because the light at the beam combiner of NPOI is dispersed over 16 spectral channels covering the wavelength range 560–870 nm, and the H $\alpha$  emission line is contained in a single 15-nm wide spectral channel, it is possible to calibrate the H $\alpha$  visibilities with respect to continuum channels. This was accomplished by adopting an angular diameter for the central star of 0.222 mas (based on the distance and radius listed in Table 1) and following the method outlined in Tycner et al. (2003) with the additional step of small channel-to-channel fixed-pattern removal (Tycner et al. 2006a) that utilized observations of two calibrator stars,  $\eta$  Aqr (for 2007, 2012, and 2014) and  $\iota$  Aqr (for 2011 and 2013).

The final calibrated interferometric data set for  $o$  Aqr from the spectral channel containing the H $\alpha$  emission line consists of a total of 994 distinct  $V^2$  measurements and these are shown in Figure 2 with the corresponding values listed in Table 2. The  $(u, v)$ -plane coverage for the entire data set is shown in Figure 3. As there is good coverage in both the N-S ( $v$  spatial frequencies) and E-W ( $u$  spatial frequencies) directions, the position angle of the disk should be reliably determined, especially as a high-axial ratio is expected from  $o$  Aqr’s shell classification.

### 3. Modelling

The parameters adopted for the central B star of the  $o$  Aqr system are given in Table 1. The spectral type of  $o$  Aqr is somewhat uncertain, usually quoted as either B7IVe (Lesh 1968) or B6IIIe (Rivinius et al. 2006).  $o$  Aqr appears in the work of Frémat et al. (2005) who determine the fundamental parameters for many Be stars accounting for gravitational darkening. Frémat et al. (2005) list “apparent” parameters of  $T_{\text{eff}} = 12,900 \pm 400\text{K}$  and  $\log g = 3.70 \pm 0.07$  and “pnrc” parameters (parameters of a non-rotating model which when spun up match the star) of  $T_{\text{eff}} = 14,560 \pm 500\text{K}$  and  $\log g = 3.99 \pm 0.08$ . One limitation of the Frémat et al. (2005) work is that the gravitational darkening formulation of Collins (1966) was used, which seems to overestimate the gravitational darkening effect. A recent reformulation of photospheric gravitational dark-

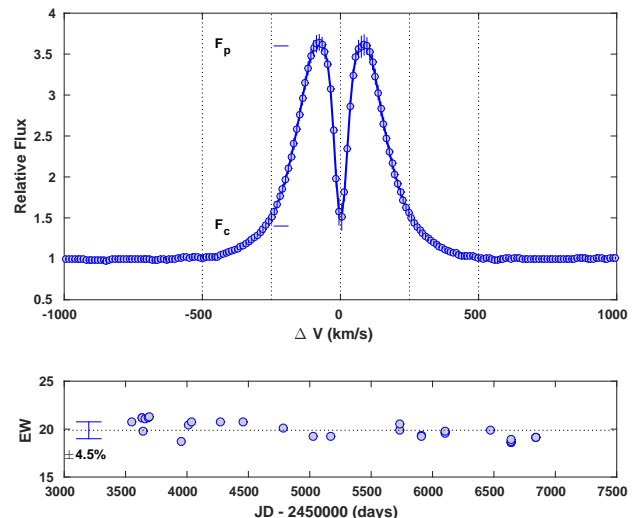


Fig. 1.— Top panel: The mean H $\alpha$  line profile of  $o$  Aqr over 2005 through 2014. The  $1\sigma$  variation is shown as the error bars. The shell parameter, defined as  $F_p/F_c$ , is 2.2, and the spectral resolving power is  $10^4$ . Bottom panel: The H $\alpha$  equivalent width as a function of the Julian date of the observations. The mean equivalent width (19.9 Å) is shown as the dotted line, and the  $1\sigma$  variation is shown as the error bar.

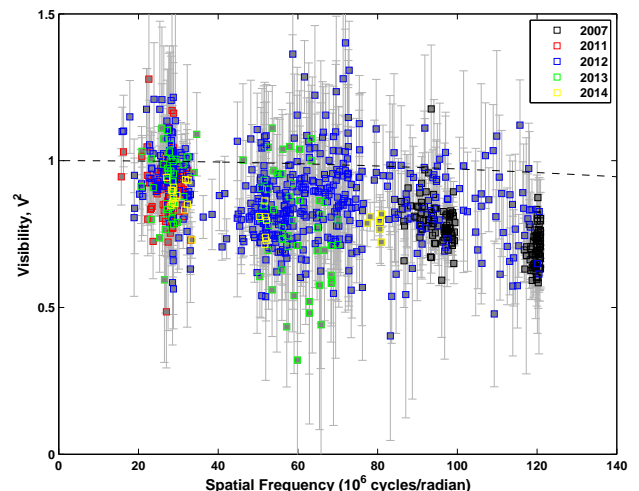


Fig. 2.— NPOI squared visibilities from the H $\alpha$  channel for  $o$  Aqr ( $N = 994$ ) as a function of the magnitude of the spatial frequency. The symbol colours indicate the observing seasons: black (2007), red (2011), blue (2012), green (2013), and yellow (2014). The signature of a central star as represented by a uniform disk with a diameter of 0.222 mas is shown as the dashed-line.

Table 2: The NPOI H $\alpha$  Interferometric Visibilities for *o* Aqr<sup>1</sup>

Julian Date (JD−2,450,000)	Spatial Frequency $u$ (10 <sup>6</sup> cycles rad <sup>−1</sup> )	Spatial Frequency $v$ (10 <sup>6</sup> cycles rad <sup>−1</sup> )	$V^2 \pm 1\sigma$	Baseline <sup>2</sup>
4264.946	77.594	61.891	0.757 $\pm$ 0.047	AN-W7
4264.946	115.830	24.900	0.699 $\pm$ 0.087	E6-W7
4264.990	69.858	61.141	0.788 $\pm$ 0.049	AN-W7
4264.990	118.350	23.709	0.749 $\pm$ 0.056	E6-W7
4265.952	76.495	61.799	0.829 $\pm$ 0.112	AN-W7
...				

<sup>1</sup> This table is available in its entirety only in the on-line journal. A portion is shown here for guidance regarding its form and content.

<sup>2</sup> The baseline entries for the NPOI instrument are explained in Armstrong et al. (1998).

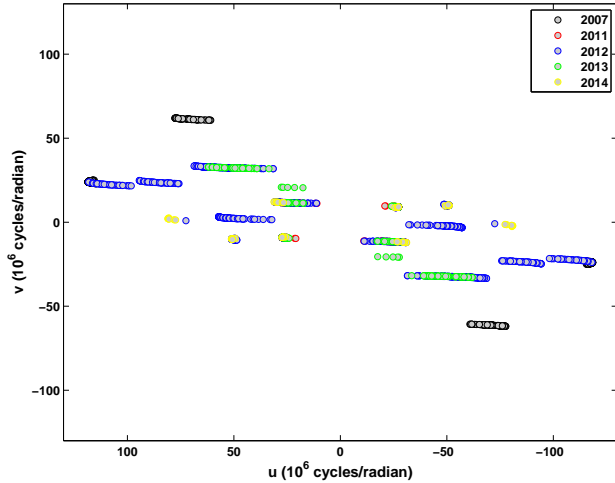


Fig. 3.— The  $(u, v)$  plane coverage for all NPOI interferometric observations. Different colours represent individual observing seasons: 2007 (black), 2011 (red), 2012 (blue), 2013 (green), and 2014 (yellow).

ening by Espinosa Lara & Rieutord (2011) gives a weaker temperature contrast between the pole and equator and better fits the available interferometric observations of rapidly rotating stars. Using the Espinosa Lara & Rieutord (2011) formalism and a rotation rate as a fraction of the critical rate of  $v_{\text{frac}} = 0.75$  (Meilland et al. 2012; Touhami et al. 2013), we find a pole to equator variation of  $T_{\text{eff}}$  of 14,600 to 12,200 K, versus 15,000 to 11,800 K for the Collins (1966) formalism. In addition, the (common) Roche geometry predicts an enhancement of the equatorial radius by  $R_e/R_p = 3.94/3.23 = 1.23$ . Given that angular diameter of the central star ( $\sim 0.2$  mas) is not expected to be spatially resolved at the baselines utilized for the current study (recall Fig. 2), we have chosen to neglect these modest effects of gravitational darkening and have treated the central star of *o* Aqr as a spherical object of uniform  $T_{\text{eff}}$ . As to the atmospheric parameters, we have adopted the default B7 parameters given by Townsend et al. (2004), which are listed in Table 1.

The BEDISK code of Sigut & Jones (2007) was used to compute the thermal structure and atomic level populations of a series of equatorial, circumstellar disks with the disk density parametrized by  $(\rho_0, n)$  in the equation

$$\rho(R, Z) = \rho_0 \left( \frac{R_*}{R} \right)^n e^{-(\frac{Z}{H})^2}. \quad (1)$$

Here  $R$  is the radial distance from the star's rotation axis and  $Z$  is the height above or below the plane of the disk. The vertical scale height of the disk is assumed to follow from hydrostatic equilibrium, parametrized by a single temperature  $T_0$  as

$$H = \left( \frac{2R_*^3 kT_0}{GM_* \mu_m m_H} \right)^{1/2} \left( \frac{R}{R_*} \right)^{3/2} \equiv H_0 \left( \frac{R}{R_*} \right)^{3/2}, \quad (2)$$

where  $M_*$  and  $R_*$  are the mass and radius of the central star, and  $\mu_m$  is the mean-molecular weight of the gas in the disk. The hydrostatic temperature for  $\alpha$  Aqr's disk, used only to fix the density scale height, was set to  $T_0 = 0.6 T_{\text{eff}} = 8,400$  K (see Sigut et al. 2009). This choice gives  $H_0/R_* = 0.029$  at the inner edge of the disk.

BEDISK models were computed for ten  $\rho_0$  values in the range  $10^{-12}$  to  $2.5 \times 10^{-10} \text{ g cm}^{-3}$  ( $\Delta \log \rho_0 = 0.266$ ) and five  $n$  values from 2.0 to 4.0 ( $\Delta n = 0.5$ ). These  $(\rho_0, n)$  values cover the range usually found for Be star disks based on H $\alpha$  spectroscopy (Silaj et al. 2010, 2014). The temperature and density structure of the disk, as well as all of the atomic level populations, were used as input to the BERAY code (Sigut 2011) which computes H $\alpha$  line profiles, SEDs, and monochromatic images on the sky, given a specified viewing angle  $i$ . BERAY works by solving the equation of radiative transfer along a series of rays directed at the observer. Rays terminating on the stellar surface use a photospheric boundary condition, either an appropriate stellar SED or photospheric H $\alpha$  profile Doppler shifted by the star's projected rotation. The circumstellar disk was assumed to be rotationally supported (i.e. in Keplerian rotation).

## 4. Results

### 4.1. H $\alpha$ Equivalent Width and Profile

Several thousand H $\alpha$  line profiles were computed covering a range in  $\rho_0$ ,  $n$ ,  $i$ , and various disk truncation radii ( $R_d$ ). H $\alpha$  profiles for the 50 combinations of  $(\rho_0, n)$  used in the BEDISK calculations were interpolated down to grid spacings of  $\Delta \log \rho_0 = 0.1$  and  $\Delta n = 0.1$ . Five disk radii were considered ( $R_d = 5, 12, 25$  and  $50 R_*$ ), along with 11 viewing inclinations, covering 0 to 90 degrees, for each model. Figure 4 shows the distribution of disk density parameters  $(n, \log \rho_0)$  that match the observed mean H $\alpha$  EW within  $2\sigma$  ( $19.9 \pm 1.8 \text{ \AA}$ ). Note that there are many values of  $R_d$  and  $i$  corresponding to each  $(n, \log \rho_0)$  pair; Figure 4 indicates a match if one or more combinations of  $R_d$  and  $i$  match the observed equivalent width range.

To further refine the model, a match to the H $\alpha$  line profile was sought. A figure of merit,  $\mathcal{F}$ , for each model profile was found by taking the average absolute fractional deviation between each model profile (convolved to a resolving power of  $10^4$ ) and an observed profile:

$$\mathcal{F} \equiv \frac{1}{N} \sum_i \frac{|F_i^{\text{mod}} - F_i^{\text{obs}}|}{F_i^{\text{obs}}}. \quad (3)$$

Here,  $F_i^{\text{mod}}$  is the model flux computed with BERAY,  $F_i^{\text{obs}}$  is the observed flux, and the sum over  $i$  is for all

$N$  wavelengths in the range  $6550 \leq \lambda_i \leq 6570$ . The minimum in  $\mathcal{F}$  then defined the best-fit model.<sup>2</sup>

Figure 5 shows the five best-fitting profiles to the first available H $\alpha$  spectrum in our series (June 26, 2005). A good match to the the peak height and central depth is obtained for the model with  $\rho_0 = 6.0 \times 10^{-12} \text{ g cm}^{-3}$ ,  $n = 2.0$ ,  $R_d = 25 R_*$  and  $i = 75^\circ$ . However, the computed models are all slightly narrower at the base of the line, and the EW of the best-fitting H $\alpha$  line profile is  $16 \text{ \AA}$ , somewhat less than that of the observed profile. Figure 4 also shows the top 17 fitting profiles in the  $(n, \log \rho_0)$  plane which have  $\mathcal{F}$  within 10% of the best-fitting model. A much narrower region is now permitted,  $-11.5 < \log \rho_0 < -11$  and  $2 < n < 2.3$ . Among the top 10% of line profile fitting models, the mode of  $i$  is  $75^\circ$  and the mode of  $R_d$  is  $25 R_*$ . The result of  $i = 75^\circ$  is consistent with the classification of  $\alpha$  Aqr as a shell star based on the H $\alpha$  shell parameter defined by Hanuschik (1996).

Fitting all available H $\alpha$  line profiles (2005-2014) results in disk parameters that vary only slightly relative to those found for the June 26, 2005 profile. All best-fit parameters are identical with the exception of  $\rho_0$  which assumes values of  $5.0 \times 10^{-12} \text{ g cm}^{-3}$ , (12 spectra),  $6.0 \times 10^{-12} \text{ g cm}^{-3}$  (10 spectra), and  $7.0 \times 10^{-12} \text{ g cm}^{-3}$  (2 spectra). The average  $\rho_0$ , weighted by the number of spectra,<sup>3</sup> is  $(5.6 \pm 0.7) \times 10^{-12} \text{ g cm}^{-3}$  where the quoted uncertainty is the  $1\sigma$  variation.

The influence of the model parameters  $\rho_0$ ,  $n$ ,  $i$  and  $R_d$  on the line profile figure-of-merit  $\mathcal{F}$  is shown in Figure 6 which plots each parameter versus  $\mathcal{F}$  in a separate panel. This results in a series of horizontal lines for each parameter value (reflecting the discrete values of that parameter considered) with the leftmost value giving the smallest  $\mathcal{F}$  achievable with that choice. For example, for  $i = 20^\circ$ , no combination of the remaining model parameters  $\rho_0$ ,  $n$ , and  $R_d$  can result in  $\mathcal{F} < 0.6$ . However, models near  $i = 75^\circ$  produce the overall minimum in  $\mathcal{F}$  of around 0.18. As illustrated in the figure, the observed line profiles discriminate most strongly in inclination, followed by  $\rho_0$ , and  $n$ . The variation of  $\mathcal{F}$  with  $R_d$  rules out small disks with  $R_d \lesssim 5 R_*$ , but the discrimination for larger disk is poor as these disks typically encompass the complete H $\alpha$  formation region, and larger disks have little impact on the relative H $\alpha$  flux profile.

<sup>2</sup>We note that other choices for the fit figure-of-merit, such as  $(F_i^{\text{mod}} - F_i^{\text{obs}})^2/\sigma$ , where  $\sigma$  is a wavelength-independent uncertainty, or  $(F_i^{\text{mod}} - F_i^{\text{obs}})^2/F_i^{\text{obs}}$ , select the same best-fitting models, with small permutations of the order. We prefer the form given in Equation 3 because equal terms indicate the same percentage deviation at each wavelength.

<sup>3</sup>A total of 24, and not 30, spectra are used because spectra taken on the same night were combined in the analysis.

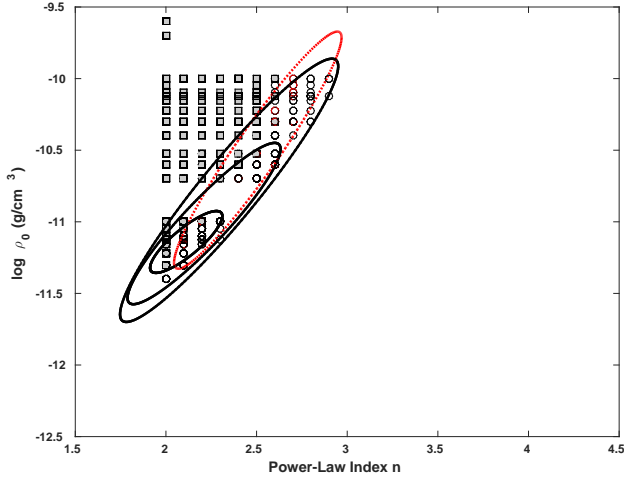


Fig. 4.— Distribution of models in the  $(n, \log \rho_0)$  plane that match the observed mean  $H\alpha$  EW within  $2\sigma$  (grey squares). Note that a square is plotted if any of the  $R_d$  or  $i$  models for a given  $n$  and  $\rho_0$  satisfy the condition. The black ellipses enclose the models (shown as open black circles) that fit the observed  $H\alpha$  profile with a figure-of-merit (Eq. 3) within 10%, 20% and 30% (in order of increasing ellipse size) of the best-fit model. The dotted red ellipse encloses the models (shown as red open circles) that fit the observed  $H\alpha$  profile with a core-weighted figure-of-merit (Eq. 4) within 10% of the best-fit model.

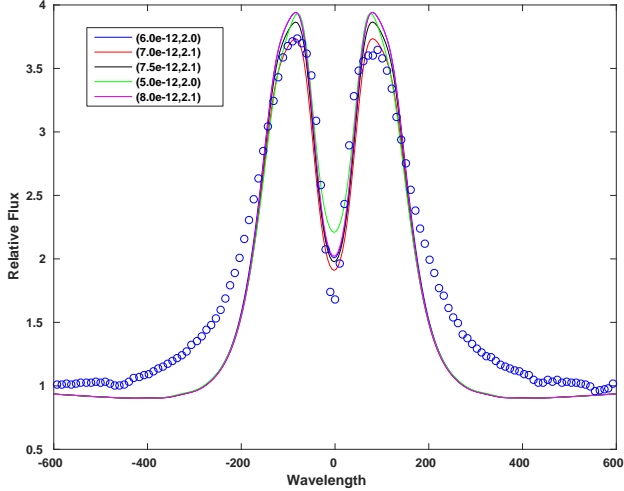


Fig. 5.— The five best-fitting  $H\alpha$  line profiles according to the figure-of-merit given by Eq. 3 (coloured lines) to the observed June 26, 2005  $H\alpha$  line profile (blue circles). The disk parameters for each of the models (base disk density and power-law index) are as indicated in the legend. All models had  $i = 75^\circ$  and  $R_d = 25 R_*$ .

The inability of our models to fit the  $H\alpha$  line wings and core simultaneously suggests that we attempt to minimize the influence of the line wings on the fitting procedure in order to gauge the effect on the models selected. To this end, we considered a revised, core-weighted, figure-of-merit,  $\mathcal{F}_{cw}$ , of the form

$$\mathcal{F}_{cw} \equiv \frac{1}{N} \sum_i w_i \frac{|F_i^{\text{mod}} - F_i^{\text{obs}}|}{F_i^{\text{obs}}}, \quad (4)$$

where the weights were chosen to be small in line wings and large in the core. The function

$$w_i \equiv \frac{F_i^{\text{obs}}}{F_c^{\text{obs}}} - 1, \quad (5)$$

where  $F_c^{\text{obs}}$  is the observed continuum flux (i.e. equal to unity as the spectra are continuum normalized) achieves this effect. Minimizing  $\mathcal{F}_{cw}$  results in best-fit profiles that better fit the line core and the top five such profiles are shown in Figure 7. Interestingly, the top model parameters now favour a higher  $\rho_0$  and larger  $n$  compared to the  $w_i = 1$  minimization. The best fit to the June, 26, 2005 profile is  $\rho_0 = 1.0 \times 10^{-10} \text{ g cm}^{-3}$  and  $n = 2.7$  for  $R_d = 25 R_*$  and  $i = 75^\circ$ . Fitting all available spectra from 2005 through 2014, and choosing the top-fitting profile in each case, gives essentially identical parameters except that  $\rho_0$  varies from  $5.0 \times 10^{-11}$  through  $1.0 \times 10^{-10} \text{ g cm}^{-3}$ . The average, weighted by the number of fitting spectra, is  $\rho_0 = (6.8 \pm 0.2) \times 10^{-11} \text{ g cm}^{-3}$ , nearly a factor of ten larger than the previous best-fit profiles based on the  $w_i = 1$  figure-of-merit.

Figure 4 also shows the selected models in the  $(n, \log \rho_0)$  plane that fit within 10% of the best-fit model; the core-weighted fits include a much wider range of models.<sup>4</sup> In conclusion, while this new weighting is arbitrary, it will become instructive when we discuss the fit to the observed near-IR SED of o Aqr in Section 4.3.

## 4.2. NPOI $H\alpha$ Interferometry

### 4.2.1. Geometric Models

We first fit two very simple geometric models to the entire set of 994 NPOI visibilities: a nearly unresolved star (represented by a uniform disk with an angular diameter of 0.222 mas) plus either a uniform elliptical or Gaussian elliptical disk representing the circumstellar contribution. If  $V_*$  is the visibility of the star and

<sup>4</sup>In contrast to Eq. (3), including models within 20% or 30% of the best model does not significantly increase the range of models in the  $(n, \log \rho_0)$  plane.

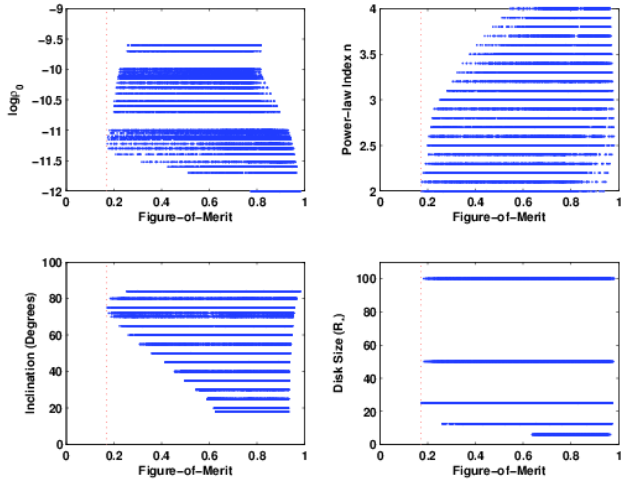


Fig. 6.— The discrimination in the  $H\alpha$  profile-fitting of the model parameters  $\rho_0$ ,  $n$ ,  $i$  and  $R_d$ . Each horizontal line represents the figures-of-merit (Eq. 3) for all models sharing that single parameter value.

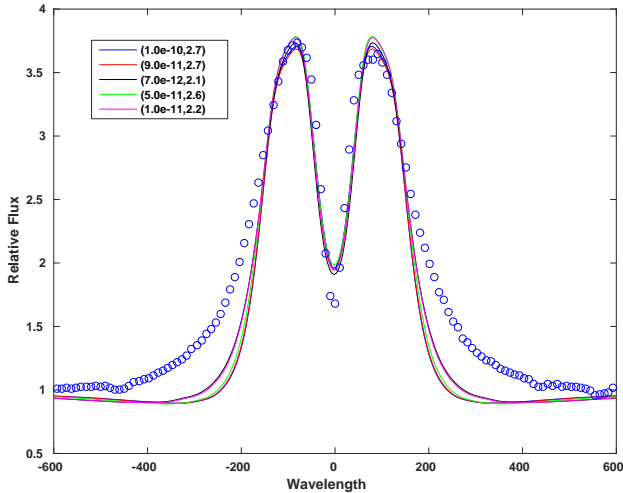


Fig. 7.— The five best-fitting  $H\alpha$  line profiles according to the core-weighted figure-of-merit given by Eq. 4 (coloured lines) to the observed June 26, 2005  $H\alpha$  line profile (blue circles). The disk parameters for each of the models (base disk density and power-law index) are as indicated in the legend. All models had  $i = 75^\circ$  and  $R_d = 25 R_*$ .

$V_D$  that of the disk, then the model visibilities can be represented as

$$V^2 = [c_* V_*(0.222 \text{ mas}) + (1 - c_*) V_D(a, b, \phi)]^2. \quad (6)$$

Here, the major and minor axis of the ellipse ( $a$  and  $b$ ), the position angle of the major axis ( $\phi$ ), and the fractional contribution of the star to the visibilities,  $0 < c_* < 1$ , are free parameters. Detailed forms for  $V_*$  and  $V_D$  for both uniform and Gaussian elliptical disks are given in Berger (2003) and Tycner et al. (2006b).

Table 3 gives the results of these fits. The star-plus-elliptical Gaussian disk fits the observations with a reduced chi-squared of  $\chi^2/\nu = 1.101$ , yielding a major axis (given by the FWHM of the Gaussian) of  $2.65 \pm 0.09 \text{ mas}$  (or equivalently a radial extent given by half-width at half-maximum of  $11.9 R_*$ ). However, the fit is unconstrained along the minor axis, consistent with  $\alpha \text{ Aqr}$  being unresolved in this dimension, and no estimate of the axial ratio is possible with this model. The position angle on the sky (measured East from North) is  $\phi = 107 \pm 6^\circ$ .

The uniform elliptical disk model produces a slightly poorer fit ( $\chi^2/\nu = 1.139$ ) and a significantly larger major axis,  $4.15 \pm 0.15 \text{ mas}$ , as expected based on the geometrically different description of the extent of the emitting region (diameter of uniform disk versus FWHM of a Gaussian). The axial ratio is found to be  $r = 0.20 \pm 0.21$ , again consistent with the minor axis not being sufficiently resolved. The position angle on the sky for this model was found to be  $\phi = 111 \pm 5^\circ$ . Finally, we note that assuming a geometrically thin disk, an axial ratio of  $r = 0.20 \pm 0.21$  implies a viewing inclination of  $i = 78 \pm 12^\circ$ , consistent with  $i = 75^\circ$  found from the  $H\alpha$  line profile modelling of Section 4.1.

A star-plus-elliptical Gaussian disk model with a fixed axial ratio of  $r \equiv 0.2$  was also tried, and this gave a reduced chi-squared of  $\chi^2/\nu = 1.097$ , just marginally better than the unconstrained fit. With this model, the major axis was  $2.58 \pm 0.09 \text{ mas}$  and the position angle on the sky,  $\phi = 110 \pm 2^\circ$ . Figure 8 compares the visibilities of this star-plus-Gaussian disk with the fixed axial ratio of  $r = 0.2$  to the NPOI observations.

In the fitting procedure,  $c_*$  was treated as a free parameter with all models finding  $c_* = 0.87$ . However, as noted by Tycner et al. (2006b),  $c_*$  is essentially

$$c_* = \frac{\Delta}{\Delta + \text{EW}_{H\alpha}} \quad (7)$$

where  $\Delta$  is the width of the NPOI filter,  $150 \text{ \AA}$ , and  $\text{EW}_{H\alpha}$  is the equivalent width of the  $H\alpha$  emission. Using  $\text{EW}_{H\alpha} = 19.9 \text{ \AA}$ , we find  $c_* = 0.88$ , in excellent agreement with the value recovered by the fits.



Touhami et al. (2013) found a major axis of  $1.525 \pm 0.642$  mas, an axial ratio of  $r = 0.249 \pm 0.059$ , and a position angle of  $\phi = 107.5 \pm 2.2^\circ$  for *o* Aqr based on K-band continuum interferometry and Gaussian elliptical fits that included the star. Their best-fit model had  $\chi^2/\nu = 1.80$ . This K-band continuum major axis found by Touhami et al. (2013) is about 50% smaller than the H $\alpha$  major axis given in Table 3.

*o* Aqr was also observed with VLT/AMBER by Meilland et al. (2012) in both the K-band continuum and Br $\gamma$ . While *o* Aqr was unresolved in the K-band, the Br $\gamma$  observations were consistent with a kinematic model with  $i = 70 \pm 20^\circ$ , a position angle of  $\phi = 120 \pm 20^\circ$ , and a disk FWHM of  $14 \pm 1$  stellar diameters. Meilland et al. (2012) note sparse  $(u, v)$  plane coverage and low S/N due to poor weather conditions. Nevertheless, the system inclination and position angle of the major axis agree with geometric models of Table 3. One interesting comparison with the current work is that the Br $\alpha$  disk FWHM found by Meilland et al. (2012) is comparable to the H $\alpha$  disk FWHM found in this work, something unusual for Be stars where the size of the H $\alpha$  region is usually 1.5 to 2 times the Br $\gamma$  region. Similar sizes for these two regions is further reflected by the very similar peak separations in the emission profiles:  $177 \text{ km s}^{-1}$  for Br $\gamma$  (Meilland et al. 2012) and  $162 \text{ km s}^{-1}$  for H $\alpha$  (Figure 1).

Finally, we note that Yudin (2001) finds an intrinsic polarization in the V Band of 0.6% for *o* Aqr with a position angle on the sky of  $+6^\circ$ . As the polarization vector is expected to be perpendicular to the major axis of the disk, this is consistent with the position angles found in Table 3.

#### 4.2.2. Physical Models

While the geometric fits of the previous section provided very good representations of the observed visibilities, they cannot constrain physical conditions in the disk, such as its density structure. To analyze the NPOI visibilities with physically-based models, the BERAY code (Sigut 2011) was used to produce images of the Be star+disk models on the sky given the observer’s viewing inclination. Each model is specified by a choice of four parameters,  $(\rho_o, n, i, \text{ and } R_d)$ , as with the H $\alpha$  spectroscopic calculations. The H $\alpha$  image computed by BERAY was integrated over a  $150 \text{ \AA}$  wavelength interval centred on H $\alpha$  to match the NPOI observations.

Given the H $\alpha$  fit results of the previous section, BERAY images were computed for disk models with  $\rho_o$  ranging from  $2.5 \times 10^{-12}$  to  $1.0 \times 10^{-10} \text{ g cm}^{-3}$  and power-law indexes  $n = 2.0, 2.25, 2.5, 2.75, \text{ and } 3.0$ .

Inclinations between  $68$  to  $80^\circ$  (in steps of  $2^\circ$ ) and  $R_d = 25$  and  $50 R_*$  were used. This subset of models includes the entire region of the best-fit H $\alpha$  profiles.

Given a computed image specified by sky intensities  $I_{ij}$ , where  $i = 1 \dots N_x^{\text{sky}}$  and  $j = 1 \dots N_y^{\text{sky}}$ , the predicted visibilities were determined by computing the discrete Fourier transform of the image following the Zernike-van Cittert theorem (e.g. see Labeyrie et al. 2006). In practice, the BERAY image was calculated with constant grid spacing on the sky within a linear region spanning  $R < 20 R_*$  and a logarithmically-spaced grid beyond that to reduce the computation time. To prepare for the DFT of the image, the outer, non-linearly spaced region was interpolated down to the constant spacing of the inner region. As this interpolation is done far away from the star and the image at these locations is smooth, linear interpolation is sufficient. All images used a final constant spacing of  $0.05 R_*$  or  $0.16 R_\odot$ . Before the DFT was computed, the image was zero-padded out to  $R = 62.5 R_*$  or  $200 R_\odot$ . The final images had  $N_x^{\text{sky}} = N_y^{\text{sky}} = 2504$ . The small grid spacing of the models gives a Nyquist frequency of  $\sim 1.8 \times 10^{10}$  cycles per radian, far larger than largest spatial frequency sampled by NPOI, and large enough so that visibility values can be expected to be negligible even for the nearly unresolved central star.

To compare with the observed visibilities, two-dimensional interpolation was performed in the DFT images at each of the observed spatial frequencies  $(u, v)$  of Figure 3. To fit the position angle of the disk, it proved more computationally efficient to rotate the  $(u, v)$  coordinates of the observed spatial frequencies, as opposed to the image itself.<sup>5</sup> The minimum in the reduced  $\chi^2$  defined the best position angle for a given image, and the minimum in reduced  $\chi^2$  over all trial images at their best-fit position angle was used to define the best model.

Over all trial images, the minimum reduced  $\chi^2$  was found to be  $\chi^2/\nu = 1.081$  ( $N = 994$ ), corresponding to the model with  $\rho_o = 5.0 \times 10^{-12} \text{ g cm}^{-3}$ ,  $n = 2.0$ ,  $R_d = 25 R_*$ . Both the  $i = 78$  and  $i = 80^\circ$  images corresponding to this model fit the data equally well, and the position angle of the major axis of these best-fit models were  $106^\circ$  and  $110^\circ$ . Thus the physical BE-DISK/BERAY models are able to fit the observed NPOI visibilities down to the limit set by the observational uncertainties and slightly better than the geometric models of Table 3. The comparison of the predicted visibilities of this best-fit model to the observed NPOI visibilities is shown in Figure 9. Also, the best-fit vis-

<sup>5</sup>We thank Ludwik Lembryk for this suggestion.



Table 3: Geometric model fits to the NPOI visibilities

Model	Major Axis (mas)	Axial Ratio	Position Angle (deg)	$c_*$	$\chi^2/\nu$
Star+					
Uniform Disk	$4.15 \pm 0.15$	$0.20 \pm 0.21$	$111 \pm 5$	$0.873 \pm 0.002$	1.139
Gaussian Disk	$2.65 \pm 0.10$	$0^a$	$107 \pm 6$	$0.870 \pm 0.003$	1.101
Gaussian Disk	$2.58 \pm 0.09$	$\equiv 0.2^b$	$110 \pm 2$	$0.864 \pm 0.003$	1.097

<sup>a</sup> The minor axis is unconstrained by the fit.

<sup>b</sup> The axial ratio is fixed at the UD result.

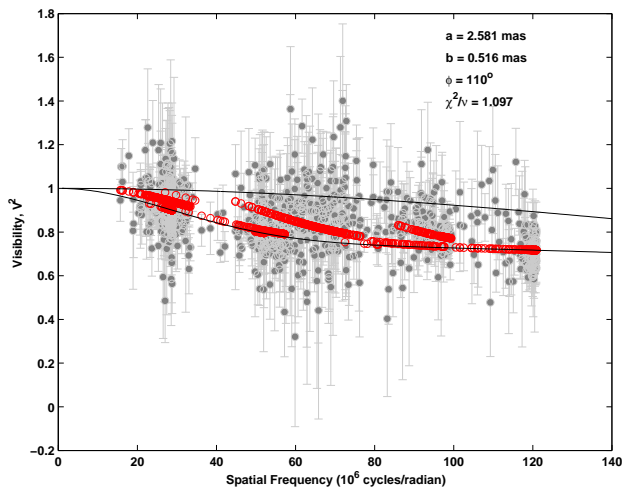


Fig. 8.— The best-fitting star-plus-elliptical Gaussian disk geometric model. The axial ratio is fixed at  $r = 0.2$ , as discussed in the text. The red symbols give the predicted model visibilities at the spatial frequencies of the observations, which are shown in light grey with  $1\sigma$  error bars. The visibilities of the major and minor axis of the model are shown as the solid lines.

ibility model is in very good agreement with the previous best-fit model for the  $H\alpha$  line profile. Table 4 summarizes the best-fit model parameters.

Figure 10 compares the observed visibilities with the best-fit disk model visibilities as a function of the magnitude of the spatial frequency. Overall, 687 of the visibilities overlap the model values within  $\pm 1\sigma$ . This results are consistent with that expected for 994 observations and  $1\sigma$  (or 68%) error bounds. The fit residuals, defined as  $z \equiv (V_{\text{obs}}^2 - V_{\text{mod}}^2)/\sigma$ , are shown as a function of spatial frequency in the lower panel of Figure 10 and as a histogram in Figure 11. The best-fit Gaussian to the residual distribution gives a mean of  $\mu = -0.107 \pm 0.065$ , and a standard deviation of  $\sigma = 1.037 \pm 0.045$ . A one-sample KS test on the cumulative distribution of the residuals and that expected from the  $N(-0.171, 1.037)$  distribution gives a p-value of 0.686, indicating the distribution is well-fit by the Gaussian. While the standard deviation of the residual distribution is consistent with 1, its mean is not consistent with 0. This small shift of the residuals could possibly be eliminated by further refining our models (i.e., finer grids in the model  $\rho_0$  and  $n$  disk density parameters), but this would not lead to much additional insight.

Figure 12 shows the location in the  $(n, \log \rho_o)$  plane of the best-fitting models based on constraints placed by the  $H\alpha$  emission profile, NPOI visibilities, and near-IR SED (discussed in the next section). The extent of the regions selected in the  $(n, \log \rho_o)$  plane reflects the fact that a number of models produce similarly good fits to both the visibilities and the  $H\alpha$  profile. For the visibilities, 104 models give a reduced  $\chi^2$  within 10% of the best fit, although it should be kept in mind that the 560 models used in the visibility analysis were deliberately chosen as a plausible sub-sample of models based on the previous fits to the  $H\alpha$  emission line profile, and many of these models differ only in their viewing inclination angle over the range 68 to 80°. The wide range of models consistent with the visibilities includes the smaller ranges consistent with the  $H\alpha$  profile at the same level.

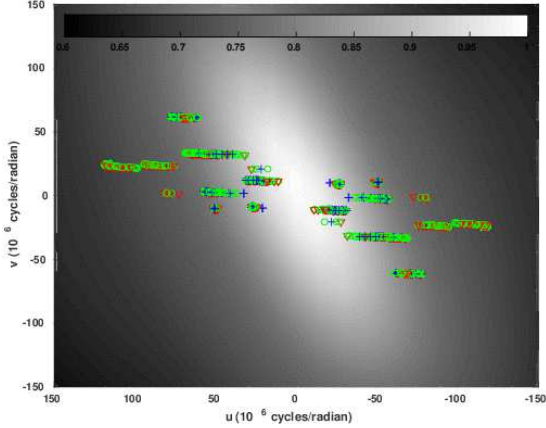


Fig. 9.— The predicted visibilities based on the Fourier transform of the best-fit model image corresponding to the disk model  $\rho_0 = 5.0 \times 10^{-12} \text{ g cm}^{-3}$ ,  $n = 2.0$ ,  $R_d = 25 R_*$ , and  $i = 78^\circ$  (grayscale, scale at top), compared to the observed visibilities (symbols). The position angle of the model is  $110^\circ$ . The symbols are: green circle (model fits to within error bars), red triangle (model below the observations), and blue plus sign (model above the observations). The overall reduced  $\chi^2$  of the fit is 1.081 for  $N = 994$ .

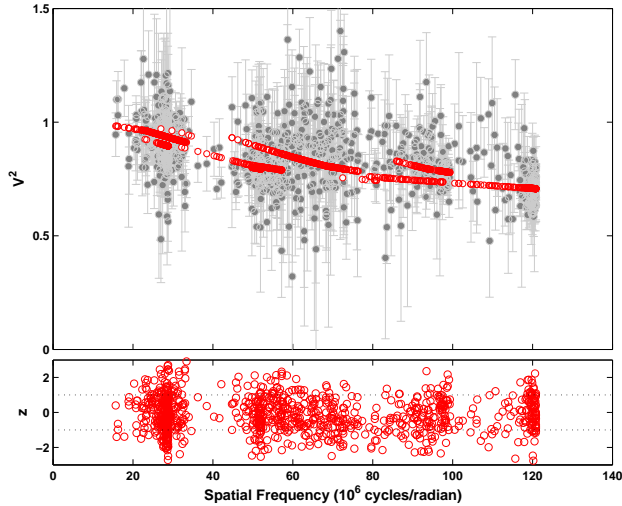


Fig. 10.— The NPOI observations with errors compared with the model visibilities based on the Fourier transform of the best-fit model image with disk parameters  $\rho_0 = 5.0 \times 10^{-12} \text{ g cm}^{-3}$  and  $n = 2.0$  as a function of the magnitude of the spatial frequency (top panel). The fit residuals,  $z = (V_{\text{obs}}^2 - V_{\text{mod}}^2)/\sigma$ , are shown in the lower panel.

Note that the diagonal trend to the best-fitting models in the  $(n, \log \rho_0)$  diagram is expected and has been noted before (Tycner et al. 2008). For an optically thick disk, the flux is, to first order, just the Planck function at the average disk temperature times the projected surface area of the disk out to  $\tau = 1$ . Therefore, the various combinations of  $\rho_0$  and  $n$  that produce similar effective emitting areas will result to first order in observational signatures that match the observations equally well.

Figure 13 shows the individual best-fit position angles averaged over all trial images with a reduced  $\chi^2$  less than a given threshold. The error bars are the  $1\sigma$  variation about this mean. For the best-fitting images,  $\chi^2/\nu < 1.15$ , the means are all consistent with  $\phi = 110 \pm 8^\circ$  which we adopt as the best estimate of the position angle of o Aqr’s disk on the sky as derived from the NPOI visibility data. This value is consistent with the position angles found from the elliptical uniform disk and Gaussian geometric models (see Table 3) which fit the visibility data almost as well as the physical model discussed here.

Figure 13 also shows that as worse-fit models are included in the average, the mean position angle rises steadily, and the  $1\sigma$  variation increases dramatically. Finally, we note that for individual images, the discrimination in position angle is good as the reduced  $\chi^2$  varies by more than factor of two over the range in  $\phi$  from 0 to  $180^\circ$ .

Given the time-span of the NPOI observations, we have also fit subsets of the visibility data. As expected, the more limited 2007 data are consistent with a significantly larger range of physical parameters. We did not analyze the 2011 data separately as it is confined to smaller spatial frequencies (see Figure 2), while analyzing the 2012-2014 data alone gives results that are indistinguishable from the full data set. Given this, it is not possible to detect variability between the 2007 and 2012-2014 data sets.

### 4.3. The Near-IR SED

Touhami et al. (2010) give optical and near-infrared fluxes (from 2008) for o Aqr at four wavelengths:  $\lambda 0.440, 0.680, 1.654$ , and  $2.179 \mu\text{m}$ . The apparent stability of o Aqr’s disk suggests that it is useful to consider these near-IR fluxes as an additional consistency check on our modelling. BERAY was used to compute optical and near-IR spectral energy distributions for the same subset of disk models used to analyze the NPOI visibilities.

To compare to the model fluxes, the Touhami et al. (2010) observations were normalized to the model SED at  $0.440 \mu\text{m}$ , and the reduced  $\chi^2$  of the fit computed for

Table 4: Summary of Best-Fit Physical Models

Feature Used to Constrain Fit	Best Fitting Parameter	$\rho_0$ ( $\text{g cm}^{-3}$ )	$n$	$R_d$ ( $R_*$ )	$i$ (degrees)	Notes
$\text{H}\alpha^a$	$\mathcal{F} = 1.85 \times 10^{-1}$	$5.0 \times 10^{-12}$	2.0	25	$75^\circ$	17 models within 10%
$\text{H}\alpha^a$ core-weighted	$\mathcal{F}_{\text{CW}} = 3.5 \times 10^{-4}$	$1.0 \times 10^{-10}$	2.7	25	$75^\circ$	10 models within 10%
$V^2$ Visibility	$\chi^2/\nu = 1.081$	$5.0 \times 10^{-12}$	2.0	25	$78 - 80^\circ$	104 models within 10%
Near-IR SED	$\chi^2/\nu = 0.296$	$1.0 \times 10^{-10}$	3.0	25	$72^\circ$	17 models with $\chi^2/\nu < 1$
Adopted	Region in Figure 12	$6.6 \times 10^{-11}$	2.7	25	$75^\circ$	

<sup>a</sup> The reported parameters are for the June, 2005 profile.

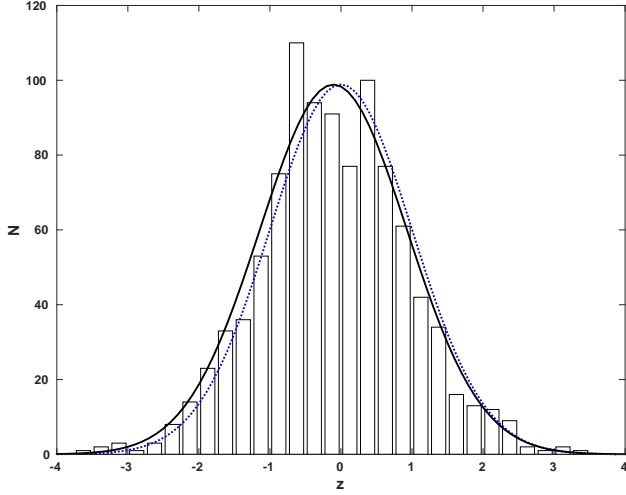


Fig. 11.— Histogram of the visibility residuals,  $z = (V_{\text{model}}^2 - V_{\text{obs}}^2)/\sigma$ , for the best-fit physical model. The solid black line shows a Gaussian fit to the residuals, giving  $\mu = -0.1065$  and  $\sigma = 1.0372$ . The dotted blue line gives the reference  $\mu = 0.0$ ,  $\sigma = 1$  Gaussian.

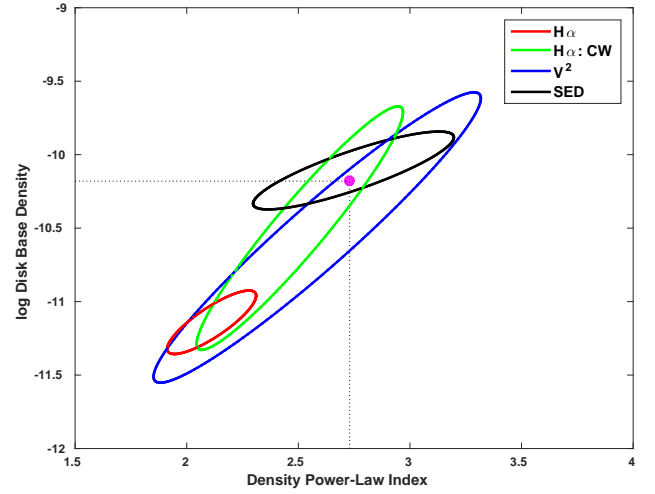


Fig. 12.— The best-fit regions in the  $(n, \log \rho_0)$  plane based on the top 10% of fits to the  $\text{H}\alpha$  emission profile (red, Eq. 3; green, Eq. 4), NPOI visibilities (blue), and Touhami et al. (2010) SED (black). The models enclosed for each feature correspond to the ‘Notes’ column in Table 4. The location of the adopted, best-fit model for o Aqr is shown as the purple circle.

the three remaining observed wavelengths. The uncertainties in the observed fluxes given by Touhami et al. (2010) are typically  $< 10\%$ , and are quoted as the quadratic sum of uncertainties due to instrumental error, errors due to repeatability of the individual observations, and errors associated with the calibration and air-mass corrections

Figure 14 shows the best fit to the observed near-IR SED. This model has  $\rho_o = 1.0 \times 10^{-10} \text{ g cm}^{-3}$ ,  $n = 3.0$ ,  $R_d = 25 R_*$ , and  $i = 72^\circ$ , and fits the observations well with a  $\chi^2/\nu = 0.49$ . Also shown in the figure is the worst-fitting model that has the same  $R_d$  and  $i$ . This is a lower-density model,  $\rho_o = 5.0 \times 10^{-12} \text{ g cm}^{-3}$  and  $n = 3.0$ , which gives fluxes close to the pure photospheric SED of the star alone. As the observed fluxes have been separately normalized to each model prediction at  $0.440 \mu\text{m}$ , the model fluxes themselves can be directly compared to each other. This illustrates that the best-fit model predicts an IR-excess and optical and UV deficits relative to the photospheric spectrum. The small deficits of  $\leq \sim 0.1$  mag are a consequence of the obscuration of the photosphere by the disk for the large viewing inclination.

In addition to this best-fit model, 17 of the 560 models considered had a reduced  $\chi^2$  of less than unity. All models consistent with the Touhami et al. (2010) SED are represented by the black ellipse in the  $(n, \log \rho_o)$  plane shown in Figure 12.

Interestingly, the near-IR SED is consistent only with the  $\text{H}\alpha$  line profile fitting when the core-weighted figure of merit is used, Equation 4. This situation is summarized in Figure 12. All three contemporaneous observational constraints, the  $\text{H}\alpha$  line profile (fit using core-weighting), the NPOI visibilities, and the Touhami et al. (2010) near-IR SED, imply a best-fit model of  $\rho_o = 6.6 \times 10^{-11} \text{ g cm}^{-3}$ ,  $n = 2.7$  with  $R_d = 25 R_*$  seen at an inclination of  $i = 75^\circ$ . These will be adopted as the disk parameters for o Aqr over the time period considered.

Figure 12 also shows that the disk parameters of the best-fit, uniformly weighted  $\text{H}\alpha$  profile (i.e., fit with Eq. 3) are not consistent with those based on the near-IR SED of Touhami et al. (2010). Nevertheless, the spatial extent of the  $\text{H}\alpha$  disk is much larger than that contributing to the near-IR flux. The extended wings of  $\text{H}\alpha$  are not fully reproduced by any of our model  $\text{H}\alpha$  profiles, and this may reflect additional material close to the star not accounted for in our assumption of a single power-law description of radial density fall-off.

#### 4.4. Disk Density Variations:

The consistency of the  $\text{H}\alpha$  equivalent width and line profile seen in Figure 1 suggests that the density in

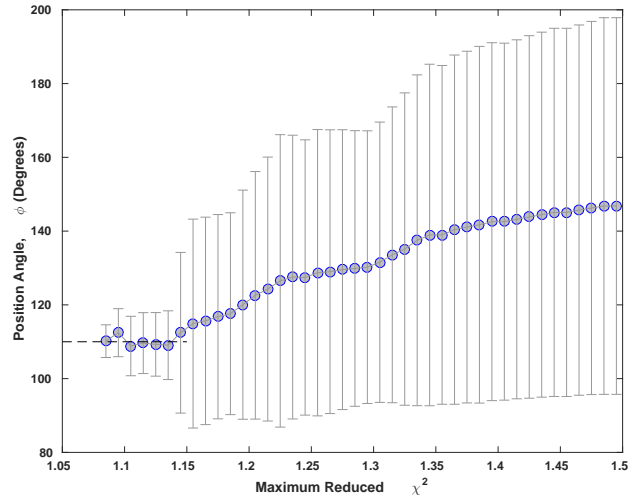


Fig. 13.— The mean position angle  $\phi$  and its  $1\sigma$  variation for all models with a reduced  $\chi^2$  less than a given maximum. A position angle of  $\phi = 110^\circ$  is shown by the horizontal dotted line, and it fits the mean position angle over all models with a reduced  $\chi^2 < 1.15$ .

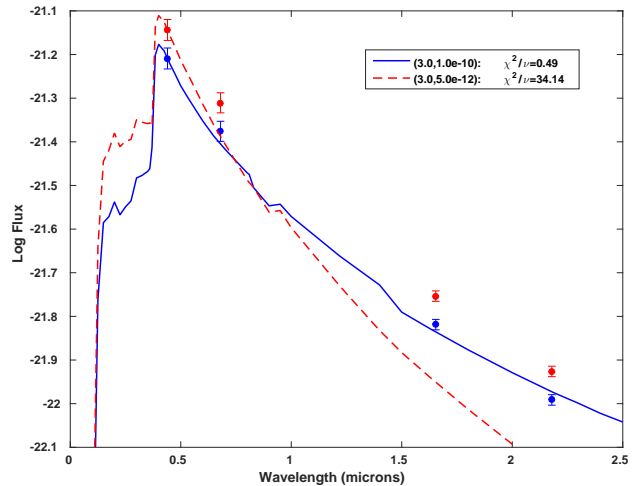


Fig. 14.— Comparison of the model SEDs with near-IR measurements of Touhami et al. (2010). The best-fit model SED, with  $n = 3.0$ ,  $\rho_o = 10^{-10} \text{ g cm}^{-3}$ ,  $R_d = 25 R_*$  and  $i = 72^\circ$ , is shown as the solid blue line. The worst-fit SED model with the same  $R_d$  and  $i$  is shown as the dotted red line. The reduced- $\chi^2$  of each model is given in the caption. Note that the observations have been separately normalized to each model's prediction at  $0.44 \mu\text{m}$ .

*o* Aqr’s disk is very stable over this time period. However it is important to understand the possible limitations of using  $H\alpha$  as a proxy for disk density stability. This is illustrated in Figure 15 which shows the equivalent width (left panel) and line profile (right panel) of  $H\alpha$  as a function of the disk base density  $\rho_0$  for the model with  $n = 2.7$ ,  $R_d = 25$  and  $i = 75^\circ$ . The maximum predicted equivalent width is  $14.1 \text{ \AA}$  at  $\log \rho_0 = -10.0$ . Near this maximum, both the  $H\alpha$  profile and equivalent width are very insensitive to changes in the disk density: for example, as the density increases from  $5.0 \times 10^{-11} \text{ g cm}^{-3}$ , the maximum increase in the equivalent width is about 10% before returning to the starting value by  $2.5 \times 10^{-10} \text{ g cm}^{-3}$ . The line profiles for  $5.0 \times 10^{-11} \text{ g cm}^{-3}$  and  $2.5 \times 10^{-10} \text{ g cm}^{-3}$  (black and blue profiles in Figure 15, respectively) are virtually identical. Thus, in this range of disk parameters, small variations in either the equivalent width or profile of  $H\alpha$  can mask large changes in the disk density.

In the current case of *o* Aqr, it is significant that disk a density model consistent with all considered observational constraints ( $H\alpha$  profile fit with core-weighting, the visibilities, and the near-IR SED) with parameters  $\rho_0 = 6.7 \times 10^{-11} \text{ g cm}^{-3}$  and  $n = 2.7$  is very near the maximum predicted model strength. This provides a natural explanation for the observed stability of the  $H\alpha$  line profile and equivalent width. As noted above, even large changes in the overall disk density, up to a factor of approximately five, will lead to only small changes in the observed  $H\alpha$  profile.

#### 4.5. The CQE Feature in Mg II $\lambda 4481$

Rivinius et al. (2006) note that *o* Aqr exhibits a central quasi-emission (CQE) feature in the core of Mg II  $\lambda 4481$ . CQE features are apparent emission “bumps” in the cores of some lines, particularly those of Mg II, He I, and Fe II. Despite their appearance as relative emission, CQEs are a pure absorption effect caused by the velocity shift (in the observer’s frame) of the local atomic line profile in a Keplerian-rotating disk viewed nearly edge-on (Hanuschik 1996). Because of this geometrical requirement, and the somewhat special circumstances of their formation, CQEs can be a useful test of a particular disk model. In this section, we show that the appearance of a CQE feature in Mg II  $\lambda 4481$  is consistent with the disk density parameters found for *o* Aqr in this work.

Rivinius et al. (2006) present a Mg II  $\lambda 4481$  profile from 1999 (somewhat outside of the time-frame of the present work) which shows a CQE feature with a central amplitude of just less than 1% ( $F_c/F_m = 1.008$  where  $F_c$  is the line centre flux and  $F_m$  is the flux minimum just outside the core; see Figure 16). To see

if this is consistent with the disk model proposed for *o* Aqr, we have used BERAY to compute Mg II  $\lambda 4481$  line profiles for circumstellar disks with  $\rho_0$  values of  $5 \times 10^{-12}$ ,  $10^{-11}$ ,  $5 \times 10^{-11}$  and  $10^{-10} \text{ g cm}^{-3}$ , all with  $n = 2.5$ ,  $R_d = 25 R_*$ , for viewing inclinations of  $i = 65^\circ$ ,  $75^\circ$ ,  $80^\circ$  and  $85^\circ$ . We have assumed an equatorial velocity of  $290 \text{ km s}^{-1}$  for *o* Aqr, corresponding to  $v_{\text{frac}} = 0.74$  (Touhami et al. 2013). Photospheric profiles were computed assuming LTE as this is a reasonable approximation at the  $T_{\text{eff}}$  of *o* Aqr (Sigut & Lester 1995).

Figure 16 shows that for  $\rho_0 = 5 \times 10^{-11} \text{ g cm}^{-3}$ , a CQE feature of the correct amplitude is predicted for  $i = 75^\circ$  and  $80^\circ$ . Interestingly, a CQE feature is not predicted for densities less than  $\rho_0 = 10^{-11} \text{ g cm}^{-3}$ . Thus the appearance of a CQE feature in Mg II  $\lambda 4481$  is consistent with the proposed disk density model found in this work and shown in Figure 12. Note that as these observations are outside time-frame considered in this work, we have not attempted to find a best-fit profile to Mg II  $\lambda 4481$ . Nevertheless, the general agreement we find is a non-trivial test of our proposed disk density model for *o* Aqr.

#### 4.6. The Mass and Angular-Momentum Content of the $H\alpha$ Disk

Combining  $H\alpha$  spectroscopy, NPOI interferometric visibilities, and the near-IR SED, we determined a best-fit disk model of  $\rho_0 = 6.6 \times 10^{-11} \text{ g cm}^{-3}$ ,  $n = 2.7$ ,  $R_d = 25 R_*$  seen at an inclination of  $i = 75^\circ$ . The position angle of the major axis on the sky was found to be  $110 \pm 8^\circ$ .

To determine the mass in the  $H\alpha$  disk implied by this model, we have computed an additional image for the best-fit parameters but for  $i = 0^\circ$ . Plotting  $2\pi R I$  versus  $R$ , where  $I$  is the model intensity at distance  $R$ , we find that 90% of the  $H\alpha$  disk light comes from  $R \leq 9.5 R_*$ . Using the best-fit disk parameters for  $(n, \rho_0)$  above and the disk density model given by Eq. (1), we find an enclosed disk mass of  $1.5 \times 10^{24} \text{ g}$  or  $\sim 1.8 \times 10^{-10} M_*$ .

Assuming Keplerian rotation for the disk, well established for Be stars (Rivinius et al. 2013), we find a total angular momentum associated with the  $H\alpha$  emitting disk of  $3.5 \times 10^{43} \text{ g cm}^2 \text{ s}^{-1}$ . The stellar angular momentum is  $J_* = \beta^2 M_* R_* V_{eq}$  where  $\beta$  is the radius of gyration,  $\sim 0.2$  (Claret & Giménez 1989), and  $V_{eq}$  is *o* Aqr’s equatorial velocity,  $290 \text{ km s}^{-1}$ . We find  $J_* = 2.2 \times 10^{51} \text{ g cm}^2 \text{ s}^{-1}$ , making the angular momentum associated with the  $H\alpha$  emitting disk  $\sim 1.6 \times 10^{-8} J_*$ .

To give an indication of the robustness of these values for the total mass and angular momentum content

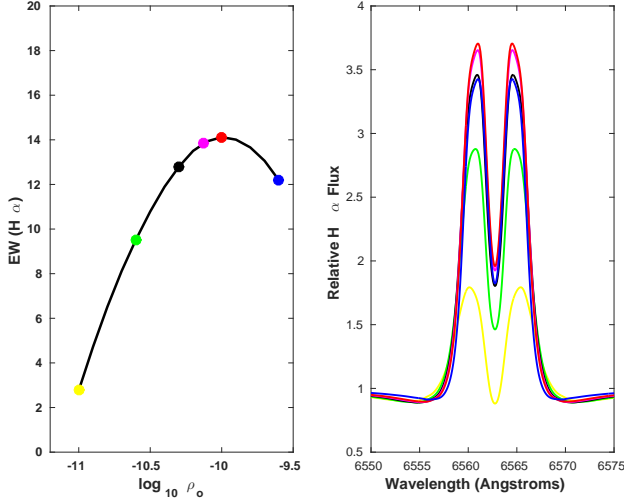


Fig. 15.— Left panel: the  $H\alpha$  equivalent width as a function of  $\rho_0$  for the model  $n = 2.7$ ,  $R_d = 25 R_*$  seen at an inclination of  $i = 75^\circ$ . Right panel: the  $H\alpha$  line profile as a function of increasing  $\rho_0$  for the same model. The  $\rho_0$  for each of the five depicted profiles corresponds to the colour of the filled circle in the left panel.

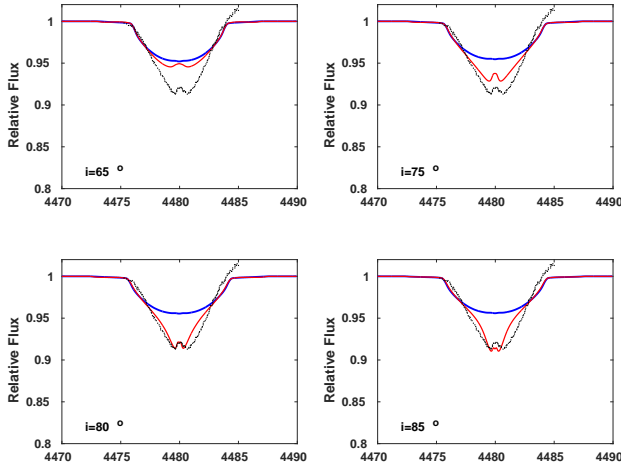


Fig. 16.—  $Mg II \lambda 4481$  line profiles for disk models with  $\rho_0 = 1 \times 10^{-11} \text{ g cm}^{-3}$  (blue) or  $\rho_0 = 5 \times 10^{-11} \text{ g cm}^{-3}$  (red) and  $n = 2.5$ ,  $R_d = 25 R_*$  and the viewing inclination indicated in each panel. The 1999 observations of Rivinius et al. (2006) are shown as the black dotted profile.

of the  $H\alpha$  emitting disk, we list in Table 5 the mass and angular momentum values for the best-fit disk models for each of the considered observational constraints separately, as given in Table 4. The disk radius that encloses 90% of the  $H\alpha$  emission is computed for each model and is given in the Table 5. The range is about a factor of three both in disk mass and five in angular momentum content. This is significantly smaller than the range in the disk base density  $\rho_0$  alone as higher densities are associated with larger values for the power-law index  $n$ .

## 5. Conclusions

We have analyzed a large set ( $N = 994$ ) of  $H\alpha$  interferometric visibilities obtained from the Navy Precision Optical Interferometer (NPOI) for the Be shell star  $\alpha$  Aqr, covering the period 2007 through 2014. Using predicted visibilities based on physical disk models computed by the BEDISK and BERAY codes, we find best-fit disk parameters that are consistent with an analysis of the  $H\alpha$  emission line profile and the near-IR SED of Touhami et al. (2010) from the same time period. We note that these physically-based BERAY images can fit the observed visibilities down to the level associated with observational uncertainties (i.e., down to the level of  $\chi^2/\nu \sim 1$ ).

The best-fit disk model with  $\rho_0 = 6.6 \times 10^{-11} \text{ g cm}^{-3}$ ,  $n = 2.7$ ,  $R_d = 25 R_*$ , implies a disk mass associated with the  $H\alpha$  emitting region of  $\sim 1.8 \times 10^{-10} M_*$  and an angular momentum content of the disk of  $\sim 1.6 \times 10^{-8} J_*$ , where  $M_*$  and  $J_*$  are the mass and angular momentum of the central  $B$  star in  $\alpha$  Aqr.

Over the nine years of  $H\alpha$  spectroscopic observations, from 2005 until 2014, we find variations in its equivalent width of typically less than 5%. However our best-fit, disk density model is at the maximum strength of  $H\alpha$  that can be produced for any value of  $\rho_0$  given a power-law index of  $n = 2.7$  seen at  $i = 75^\circ$ . For this model, variations in the disk density,  $\rho_0$ , of up to a factor of  $\sim 5$  would not lead to noticeable changes in the  $H\alpha$  equivalent width or its profile and variations of this magnitude cannot be excluded over the time period considered.

We further test our model by comparing to the 1999 CQE feature in  $Mg II \lambda 4481$  observed by Rivinius et al. (2006) and find that very similar feature can be produced by our best-fit disk density model, representing an additional and highly non-trivial success of our modelling.

Finally, we note that in order to produce fits to the  $H\alpha$  line profile consistent with the other constraints, the fits needed to be weighted more heavily in the line core (emission peaks and central depression) at the ex-

Table 5: Summary of disk mass and total angular momentum content.

Diagnostic	$(R_{90}/R_*)^a$	$M_d$ (gm)	$M_d/M_*$	$J_d$ (g cm <sup>2</sup> s <sup>-1</sup> )	$J_d/J_*$
H $\alpha$ ( $\mathcal{F}$ )	19.5	$1.0 \times 10^{+24}$	$1.2 \times 10^{-10}$	$3.7 \times 10^{+43}$	$1.7 \times 10^{-8}$
H $\alpha$ ( $\mathcal{F}_{CW}$ )	8.3	$2.0 \times 10^{+24}$	$2.3 \times 10^{-10}$	$4.4 \times 10^{+43}$	$2.0 \times 10^{-8}$
$V^2$	19.5	$1.0 \times 10^{+24}$	$1.2 \times 10^{-10}$	$3.7 \times 10^{+43}$	$1.7 \times 10^{-8}$
near-IR SED	3.3	$5.8 \times 10^{+23}$	$6.9 \times 10^{-11}$	$9.0 \times 10^{+42}$	$4.2 \times 10^{-9}$
Adopted <sup>b</sup>	9.5	$1.5 \times 10^{+24}$	$1.8 \times 10^{-10}$	$3.5 \times 10^{+43}$	$1.6 \times 10^{-8}$

<sup>a</sup>  $R_{90}$  is the disk radius that encloses 90% of the integrated H $\alpha$  light.

<sup>b</sup> This is the best-fit model to all three constraints (H $\alpha$  ( $\mathcal{F}_{CW}$ ),  $V^2$ , and near-IR SED) shown in Figure 12.

pense of the line wings. This may reflect the limitation of the assumption of a single power-law for the disk’s equatorial density.

We would like to thank the anonymous referee and Doug Gies for many helpful comments. This work is supported by the Canadian Natural Sciences and Engineering Research Council (NSERC) through a Discovery Grant to TAAS and by CMU through a FRCE Type B grant to CT. We would like to thank the NPOI project staff for their support in acquiring the interferometric data used in this work, and Brennan Kerkstra and Sandeep Chiluka for assistance with NPOI data reductions. The Navy Precision Optical Interferometer is a joint project of the Naval Research Laboratory and the US Naval Observatory, in cooperation with Lowell Observatory and is funded by the Office of Naval Research and the Oceanographer of the Navy. We thank the Lowell Observatory for the telescope time used to obtain the H $\alpha$  line spectra presented in this work.

*Facilities:* NPOI, Hall (Solar Stellar Spectrograph)

## REFERENCES

- Armstrong, J. T., Mozurkewich, D., Rickard, L. J., et al. 1998, *ApJ*, 496, 550
- Bagnulo, S., Landstreet, J. D., & Kochukhov, O., 2012, *A&A* 538, 129
- Berger, J.-P., 2003, *Observing with the VLTI*, EAS Pub. Series, 6, G. Perrin & F. Malbet, editors, 23
- Claret, A., & Giménez, A., 1898, *A&AS* 81, 37
- Collins, G. W. II 1966, *ApJ*, 146, 914
- Cutri, R. M., Skrutskie, M. F., van Dyk, S., et al., 2003, *CDS/ADC Collection of Electronic Catalogues*, 2246, 0
- Espinosa Lara, F., & Rieutord, M., 2011, *A&A*, 533, A43
- Frémat, Y., Zorec, J., Hubert, A.-M., & Floquet, M., 2005, *A&A* 440, 305
- Grundstrom, Erika D., & Gies, Douglas R., 2006, *ApJ*, 651, L53.
- Hanuschik, R. W., Hummel, W., Dietle, O., & Sutorius, E., 1995, *A&A*, 300, 173.
- Hanuschik, R. W. 1996, *A&A*, 308, 170
- Hall, J. C., Fulton, E. E., Huenemoerder, D. P., Welty, A. D., & Neff, J. E. 1994, *PASP*, 106, 315
- Haubois, X., Carciofi, A. C., Rivinius, Th., Okazaki, A. T., & Bjorkman, J. E. 2012, *ApJ*, 756, 156
- Howarth, I., D., 2007, in *Active OB Stars: Laboratories for Stellar and Circumstellar Physics*, ed. Stefl, S., Owocki, S., & Okazaki, T. ASP Conference Series 361, 15
- Hubrig, S., et al., 2009, *AN*, 330, 708.
- Hummel, C. A., Mozurkewich, D., Armstrong, J. T., et al. 1998, *AJ*, 116, 2536
- Hummel, C. A., Benson, J. A., Hutter, D. J., et al., 2003, *AJ*, 125, 2630
- Hummel, C. A. 2008, *New A Rev.*, 52, 167
- Jones, C. E., Tycner, C., Sigut, Benson, J. A., & Hutter, D. J., 2008, *ApJ*, 687, 598
- Labeyrie, A, Lipson, S.G., & Nisenson, P., 2006, *An Introduction to Optical Stellar Interferometry*, Cambridge University Press, New York
- Lesh, Janet Rountree, 1968, *ApJS*, 17, 371
- Meilland, A., Millour, F., Kanaan, S., Stee, Ph., Hofmann, K.-H., Natta, A. & Perraut, K, 2012, *A&A*, 538, A110.
- Okazaki, T., 1991, *PASJ*, 43, 75
- Oudmaijer, R. D., & Parr, A. M., 2010, *MNRAS* 405, 2439
- Perryman, M. A. C., Lindegren, L., Kovalevsky, J., et al. 1997, *A&A*, 323, L49
- Poeckert, R., & Marlborough, J. M., 1979, *ApJ* 233, 259
- Porter, John M., & Rivinius, T. 2003, *PASP*, 115, 1153
- Press, W. H., Teukolsky, S. A., Vetterling, W. T., & Flannery, B. P., 1992, *Numerical Recipes in Fortran*, Cambridge University Press, New York
- Rivinius, T., 2013, *Astrophys Space Sci Proc.* 31, 253
- Rivinius, T., Carciofi, Alex C., & Martayan, C. 2013, *A&A Review*, 21, 69



- Rivinius, Th., Stefl, S., & Baade, D. 2006, A&A 459, 137
- Sigut, T.A.A., & Jones, C.E. 2007, ApJ, 668, 481
- Sigut, T.A.A., McGill, M.A., Jones, C.E. 2009, ApJ, 699, 1973
- Sigut, T.A.A. 2011 IAU Symp. 272, “Active OB Stars: Structure, Evolution, Mass-Loss, and Critical Limits,” Neiner, C., Wade, G., Meynet, G., & Peters, G. (eds), 426
- Sigut, T. A. A., & Lester, J. B., 1995, ApJ, 461, 972
- Silaj, J., Jones, C. E., Sigut, T. A. A., Tycner, C., 2014, ApJ, 795, 82.
- Silaj, J., Jones, C. E., Tycner, C., Sigut, T. A. A., & Smith A., D., 2010, ApJS, 187, 228.
- Stoeckley, T. R., & Buscombe, W., 1987, MNRAS, 227, 801
- Tycner, C., Hajian, A. R., Mozurkewich, D., et al. 2003, AJ, 125, 3378
- Tycner, C., et al., 2005, ApJ, 624, 359
- Tycner, C., Benson, J. A., Hutter, D. J., Schmitt, H. R., & Zavala, R. T. 2006a, Proc. SPIE, 6268, 626849
- Tycner, C., Gilbreath, G. C., Zavala, et al., 2006b, AJ, 131, 2710
- Tycner, C., Jones, C. E., Sigut, T. A. A., Schmitt, H. R., Benson, J. A., Hutter, D. J., & Zavala, R. T., 2008, ApJ, 689, 461
- Touhami, Y., Richardson, N. D., Gies, D. R., et al. 2010, PASP, 122, 379
- Touhami, Y., Gies, D. R., Schaefer, G. H., et al., 2013, ApJ, 768, 128
- Townsend, R. H. D., Owocki, S. P., & Howarth, I. D. 2004, MNRAS, 350, 189
- Yudin, R. V., 2001, A&A, 368, 912